Edith Cowan University

Research Online

Research outputs 2022 to 2026

4-6-2023

Experimental and computational fluid dynamics investigation of mechanisms of enhanced oil recovery via nanoparticle-surfactant solutions

Nurudeen Yekeen
Edith Cowan University

Ali Masoud Ali Elakkari

Javed Akbar Khan

Muhammad Ali

Ahmed Al-Yaseri

See next page for additional authors

Follow this and additional works at: https://ro.ecu.edu.au/ecuworks2022-2026

 Part of the Engineering Commons

10.1021/acs.energyfuels.3c00136
Yekeen, N., Ali Elakkari, A. M., Khan, J. A., Ali, M., Al-Yaseri, A., & Hoteit, H. (2023). Experimental and computational fluid dynamics investigation of mechanisms of enhanced oil recovery via nanoparticle-surfactant solutions. *Energy & Fuels*, 37(7), 5114-5129. https://doi.org/10.1021/acs.energyfuels.3c00136
This Journal Article is posted at Research Online.
https://ro.ecu.edu.au/ecuworks2022-2026/2280

Authors

Nurudeen Yekeen, Ali Masoud Ali Elakkari, Javed Akbar Khan, Muhammad Ali, Ahmed Al-Yaseri, and Hussein Hoteit

This journal article is available at Research Online: https://ro.ecu.edu.au/ecuworks2022-2026/2280

energy&fuels

pubs.acs.org/EF

Article

Experimental and Computational Fluid Dynamics Investigation of Mechanisms of Enhanced Oil Recovery via Nanoparticle-Surfactant Solutions

Nurudeen Yekeen,* Ali Masoud Ali Elakkari, Javed Akbar Khan, Muhammad Ali,* Ahmed Al-Yaseri, and Hussein Hoteit

Cite This: *Energy Fuels* 2023, 37, 5114−5129

Read Online

ACCESS | Metrics & More | Article Recommendations | Supporting Information

ABSTRACT: The enhancement in surfactant performance at downhole conditions in the presence of nanomaterials has fascinated researchers' interest regarding the applications of nanoparticle-surfactant (NPS) fluids as novel enhanced oil recovery (EOR) techniques. However, the governing EOR mechanisms of hydrocarbon recovery using NPS solutions are not yet explicit. Pore-scale visualization experiments clarify the dominant EOR mechanisms of fluid displacement and trapped/residual oil mobilization using NPS solutions. In this study, the influence of multiwalled carbon nanotubes (MWCNTs), silicon dioxide (SiO_2), and aluminum oxide (Al_2O_3) nanoparticles on the EOR properties of a conventional surfactant (sodium dodecyl benzene sulfonate, SDBS) was investigated via experimental and computational fluid dynamics (CFD) simulation approaches. Oil recovery was reduced with increased temperatures and micromodel heterogeneity. Adding nanoparticles to SDBS solutions decreases the fingering and channeling effect and increases the recovery factor. The simulation prediction results agreed with the experimental results, which demonstrated that the lowest amount of oil (37.84%) was retained with the micromodel after MWCNT-SDBS flooding. The oil within the micromodel after Al_2O_3-SDBS and SiO_2-SDBS flooding was 58.48 and 43.42%, respectively. At 80 °C, the breakthrough times for MWCNT-SDBS, Al_2O_3-SDBS, and SiO_2-SDBS displacing fluids were predicted as 32.4, 29.3, and 21 h, respectively, whereas the SDBS flooding and water injections at similar situations were at 12.2 and 6.9 h, respectively. The higher oil recovery and breakthrough time with MWCNTs could be attributed to their cylindrical shape, promoting the MWCNT-SDBS orientation at the liquid−liquid and solid−liquid interfaces to reduce the oil−water interfacial tension and contact angles significantly. The study highlights the prevailing EOR mechanisms of NPS.

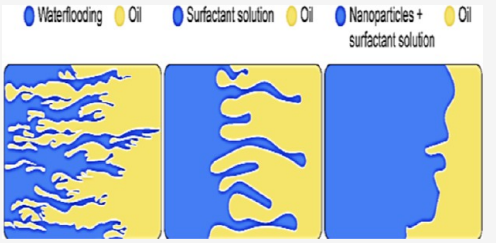

1. INTRODUCTION

Global energy consumption is increasing due to the increasing world population and rapid development in all life aspects. A 30% increment in energy consumption compared to the current global energy demand is expected by 2030.[1−3] Fossil fuels remain the most critical energy source worldwide; however, only a few hydrocarbon-producing reservoirs have been discovered within the last few decades. Hence, hydrocarbon recovery from existing reservoirs must be improved to offset the mismatch between energy demand and supply.

Surfactant flooding is a popular enhanced oil recovery (EOR) method[4] to achieve lower residual oil saturation in a hydrocarbon reservoir by increasing the capillary number and the dominance of viscous forces over the capillary forces.[5] Surfactant molecules are surface-active agents that adsorb at the oil−water interfaces to decrease the interfacial tension (IFT) between fluids in the rock pores and alter the rock-wetting state from a hydrophobic condition to a hydrophilic state.[6,7]

However, surfactant molecules are easily lost on the rock surfaces, especially when the charges of the surfactants and rock surfaces are different, resulting in the increased cost of trapped oil mobilization via surfactant flooding. Moreover, field applications of surfactant flooding are not as successful as the laboratory results suggested due to surfactant intolerance to high-salinity and high-temperature downhole conditions.[8]

Nanoparticles have recently attracted considerable research interest concerning improving the stability and surfactant performance at subsurface conditions.[4] Nanoparticles are robust and more stable at high temperatures and in formation of brines. They have a high surface area due to their small size, and their surface wettability can be controlled to offer more versatility and improvement in macroscopic and microscopic sweep efficiency during nanoparticle-surfactant (NPS) fluid flooding.[8] In previous studies, the EOR applications of nanotechnology have been discussed with respect to nanofluid

Received: January 11, 2023
Revised: March 14, 2023
Published: March 21, 2023

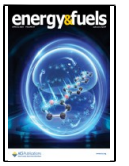

Downloaded via EDITH COWAN UNIV on May 5, 2023 at 03:26:30 (UTC).
See https://pubs.acs.org/sharingguidelines for options on how to legitimately share published articles.

ACS Publications

© 2023 American Chemical Society

https://doi.org/10.1021/acs.energyfuels.3c00136
Energy Fuels 2023, 37, 5114−5129

synthesis, production of nanoemulsions through nanoparticles/surfactants, and the utilization of active metals as nanocatalysts for in situ enhancement of heavy oil cuts.[9] Yang et al.[10] showed that when the titania nanoparticle surface was modified with oleic acid, the nanoparticles demonstrated significant tendency to promote hydrocarbon recovery from low-permeable reservoirs and reduce the injection pressure.

Generally, nanomaterials are materials with any of the external dimensions or internal structures in the nanoscale, that is, 100 nm or less.[11] They can be categorized into nanoclays, nanoemulsions, and nanoparticles and can come in various shapes such as tubular, spherical, cylindrical, and irregular, with organic and inorganic classifications such as nanosilica (SiO_2 nanoparticles), carbon nanotubes, and nanoalumina (Al_2O_3 nanoparticles).[12] Surfactants are unstable at reservoir conditions, whereas nanoparticles are not as surface-active as surfactant molecules and cannot reduce contact angles and oil−water IFT to ultralow conditions, as demonstrated by surfactants.[13]

Thus, the synergy of nanoparticles and surfactants has been identified as an ideal solution for optimum hydrocarbon recovery. Surfactant molecules augment the nanoparticles in oil−water IFT reduction and wettability alterations, whereas solid nanoparticles are tolerant to high-salinity brine and assist the surfactant in surviving at unfavorable high-temperature and high-pressure subsurface conditions.[14] Prior studies have demonstrated that the synergy of conventional surfactants, such as sodium dodecyl sulfate and sodium dodecyl benzene sulfonate (SDBS), and nanoparticles, such as SiO_2 and Al_2O_3 nanoparticles, has a higher EOR potential compared to surfactant solutions or nanofluids alone.[15−20]

Moreover, SiO_2 and Al_2O_3 nanoparticles are the most widely applied for EOR operations. SiO_2 nanoparticles are popular choices for recovering trapped hydrocarbons from sandstone reservoirs, whereas Al_2O_3 nanoparticles are favorable options for carbonate reservoirs. Similar negative charges on nanosilica and sandstone reservoir rock surfaces and similar positive charges on nanoalumina and carbonate reservoir rocks ensure that the injected fluids reach the targeted trapped oil without being adsorbed on the rock surfaces.[21,22]

Previous research has revealed that the loss of surfactant molecules onto rock surfaces is reduced with SiO_2 and Al_2O_3 nanoparticles due to the competitive adsorption of the surfactant molecules onto the rock and nanoparticle surfaces.[21,23−28] Thus, lower concentrations of surfactants are required during NPS flooding at reservoir conditions. Nanoparticles have different shapes that can influence their performance as EOR agents. For instance, multiwalled carbon nanotubes (MWCNTs) are cylindrical compared to the almost spherical SiO_2 and Al_2O_3 nanoparticles. Apart from the nanoparticle's concentration and sizes, the nanoparticle geometry and shape could influence the adsorption and orientation of the particles at the liquid−liquid and solid−liquid interfaces.[29−31]

Researchers have recently expressed substantial interest in the applications of carbon nanotubes for EOR due to their outstanding characteristics, such as high mechanical strength, conductivity, and superior aspect ratios, which are pertinent for downhole operations.[32] Research has revealed drastic reductions in oil−water IFT and rock hydrophobicity in the presence of nanofluids formed from dispersed carbon nanotubes in various base fluids and surfactants.[29,32−34] Carbon-nanotube-stabilized emulsions and foams were also reported to be more stable than those stabilized with SiO_2 and Al_2O_3 nanoparticles.[30,35−39] Moreover, the interaction of injected carbon-nanotube nanofluids with acidic oil results in the formation of in situ surfactants, aiding in the mobilization of trapped oil by reducing the capillary pressure in the rock pores.[32]

Specifically, Razavinezhad et al.[34] recently reported that, although the surfactant-polymer solution reduced the contact angles of oil-wet glass from 143.6 to 24°, the contact angle reduced to zero, and the oil recovery increased by 5−11% in carbon nanotube-surfactant solutions. Li et al.[36] found that durable foam was formed by the synergy of the SDBS and hydroxylated MWCNTs due to the adsorption of the surfactant-modified hydroxylated MWCNTs at the foam lamellae. This phenomenon increased the foam film's thickness and dilatational viscoelasticity. Likewise, the generated foam could plug the macrofractures in low-permeable cores.[40]

Haq et al.[41] assessed the synergistic influence of a green surfactant (alkyl polyglycoside) and carbon particles (date leaf carbon particles and carbon nanotubes) on oil recovery. They found that the optimum formulation (based on IFT measurements) achieved 89% recovery of the initial oil in place and 45% tertiary recovery.[42]

Although some studies have been conducted on application of the synergy of nanoparticles and surfactants for EOR, most previous research has been limited to macroscopic experiments, and the governing pore-scale mechanisms of hydrocarbon recovery via the synergy of surfactants and nanoparticles have not been fully explored. Thus, this study was conducted to elucidate the mechanisms of EOR using NPS solutions.

Microscopic assessments of interactions between the NPS solutions and resident oil in the porous media were conducted via experiments and computational fluid dynamics (CFD) techniques. First, field-emission scanning electron microscopy (FESEM) and energy-dispersive X-ray (EDX) analyses were conducted to characterize the nanoparticle morphology and compositions. Then, we prepared the NPS solutions and measured their effects on decane-oil−water IFT and wettability (contact angles). Afterward, micromodel flooding and CFD simulations were performed to elucidate the mechanisms of residual oil mobilization and recovery.

The pore-scale visualization of displacing−displaced fluid interactions in etched glass micromodels provides insights into the mechanisms of hydrocarbon recovery using NPS solutions. Resident oil mobilization using MWCNTs and a popular EOR surfactant (sodium dodecyl benzene sulfonate, SDBS) was compared to that for the SDBS solution only, water-flooding, and Al_2O_3/SDBS and SiO_2/SDBS mixed systems. The oil−water IFT between the different NPS solutions and decane and the contact angles of the NPS droplets on rock surfaces were measured using a spinning drop tensiometer and drop-shape analyzer (DSA 25). The IFT data and contact angle data sets were used to explain the pore-scale microscopic observations from the experiments and CFD simulation results.

The CFD is a versatile technique for conducting computer-based simulations of fluid flow at velocity profile, flow rate, temperature, pressure distributions, and other conditions that are almost impossible, time-consuming, or hazardous to simulate through laboratory experiments.[43,44] The CFD simulation permits a visual evaluation of the fluid flow behavior and phase-displacement characteristics in porous media at the reservoir scale. Unlike conventional software, such

https://doi.org/10.1021/acs.energyfuels.3c00136
Energy Fuels 2023, 37, 5114−5129

Table 1. Summary of Experiments[a]

tests	purposes	experimental approach
nanomaterial characterization	to describe the morphology and identify the main components of nanomaterials	the FESEM and EDX analyses were conducted with a field-emission scanning electron microscope; XRF analysis was conducted with WDXRF
oil−water IFT measurement	to study the influence of NPS solutions on the IFT between water and decane	the IFT was measured using a spinning drop tensiometer
contact angle measurement	to assess the capacity of the NPS solution to alter the wettability of the porous medium to hydrophilic conditions	contact angles were measured with a drop-shape analyzer
pore-scale visualization experiments	to identify the pore-scale mechanisms of resident oil mobilization and recovery using NPS solutions	NPS flooding using 2D etched micromodels was conducted at various conditions
CFD simulation	to elucidate the mechanisms of oil recovery using NPS solutions at reservoir conditions	the CFD simulation was conducted using Ansys 2021 R2 (Fluent Inc.) CFD software

[a]Notes: CFD, computational fluid dynamics; FESEM, field-emission scanning electron microscopy; IFT, interfacial tension; NPS, nanoparticle surfactant; EDX, energy-dispersive X-ray; XRF, X-ray fluorescence; WDXRF, wavelength-dispersive X-ray fluorescence.

as black oil/composition models that consider the porous media as a black box, pore-network modeling difficulties can be easily solved through CFD. Moreover, several parameters can be investigated more economically than in laboratory experiments.[43]

2. EXPERIMENTAL SECTION

Five sets of experiments were conducted in this study to achieve the objective. The tests and experimental approaches are summarized in Table 1.

2.1. Materials. An anionic surfactant with multipurpose applications in oilfields and industries, SDBS was procured from Sigma-Aldrich and used as the surfactant for the Experimental Section. The SDBS was 99% pure with a molecular weight of 348.48 g/mol. Normal decane ($C_{10}H_{22}$, from Acros Organics) and crude oil (West Lutong from Sarawak) were the two types of oils used for this research. Decane was used for oil−water interfacial tension measurements, whereas crude oil was used for microscopic experiments. We could not use crude oil for the oil−water interfacial measurement because the carbon nanotube solution and oil were black, and it is difficult to see the spinning drop clearly.

The viscosities of the oil were measured using an RST rheometer (product of Brookfield Engineering) as 10 cp and 0.94 cp for the crude oil and normal decane, respectively. The density was measured as 0.83 g/cm^3 (for crude oil) and 0.73 g/cm^3 (for normal decane) at room conditions. The sample preparation was performed with ultrapure water. The crude oil composition from the saturate, aromatic, resin, and asphaltene (SARA) analysis is presented in Table 2, and the details of the nanoparticles used for the research are presented in Table 3. All nanomaterials were more than 98% pure.

Table 2. Saturate, Aromatic, Resin, and Asphaltene Analysis of West Lutong Crude

parameters	mass (%)
saturates	10.99
volatiles	79.12
resins	6.26
asphaltenes	0.01
aromatics	2.66
inorganics	0.05

2.2. Characterizations and Solution Preparations. A field-emission scanning electron microscope (SUPRA 55VP; Carl Zeiss Germany) was used along with EDX spectroscopy to describe the nanomaterial morphology and sample compositions.[12] The FESEM and EDX results of the nanomaterials used for this research are presented in Figure 1.

The nanoparticle morphology presented in Figure 1 reveals that Al_2O_3 and SiO_2 nanoparticles are almost spherical, whereas the shape of the MWCNTs is quite cylindrical. The X-ray fluorescence (XRF) analysis of the rock substrate was determined using a wavelength-dispersive XRF (WDXRF) spectrometer (model: S4 Pioneer), a product of Bruker AXS company (Karlsruhe, Germany). The XRF analysis demonstrated that the main composition of the rock sample is SiO_2 (Table 4).

The nanoparticles and surfactants in this research were all solid; thus, the solutions were prepared by directly weighing the preferred mass (in grams) and dispersing it in water (100 mL). Each solution was mixed using a magnetic stirrer for 30 min. Nanoparticles tend to agglomerate in solutions; therefore, a QSonica sonicator (Q500) was used at 500 W and 20 kHz to disperse nanoparticles in the surfactant solution to prevent agglomeration. In addition, 0.1 wt % SDBS, representing a concentration above the critical micelle concentration of SDBS, was used for solution preparations. The critical micelle concentration of SDBS has been reported as 0.045 wt % in previous studies.[29,45]

The Al_2O_3 and SiO_2 concentrations varied from 0.1 to 1.0 wt %, whereas the MWCNT concentrations varied from 0.01 to 0.1 wt % because of their high agglomeration tendency. However, the values of 0.1 wt % Al_2O_3 and SiO_2 and 0.01 wt % MWCNTs were chosen for further experiments because pore-plugging could occur at higher concentrations.[46−48]

2.3. Interfacial Tension Experiments. The spinning drop approach measured the IFT between the oil and nanofluid/NPS solutions at 303.15, 323.15, and 353.15 K. The major components of the spinning drop tensiometer (SVT 20N, a product of DataPhysics Instruments, Germany) include a high-resolution camera (as part of the monitoring systems), a capillary tube, and devices for fluid injection (syringe and needle). The desired solution concentration was injected into a rotating horizontal tube at the speed of almost 4,000 rpm to measure the oil−water IFT. A centrifugal force was created by the rotating horizontal tube toward the tube walls, resulting in the deformation of the drop of liquid into an elongated shape. The lengthening of the liquid drop stops when the centrifugal forces become equal to the IFT. The drop-shape at the equilibrium point represents the oil−water IFT.

2.4. Wettability Experiments. The wetting capacity of NPS solutions was determined by measuring the static contact angles of sessile droplets of the respective solutions on the rock surface ($L \times W \times H = 2 \times 2 \times 0.3$ cm). The measured static contact angle was achieved by creating a solution drop (5 ± 1 μL) through a hanging metal syringe needle (0.515 mm diameter). The droplet was brought into contact with a rock surface polished with silicon carbide abrasive paper. After contact, the droplets detached from the metallic syringe and spread on the rock surface. The dispersed droplet images were processed using advanced surface science software. An average of 10 contact angle measurements was taken to ensure the accuracy and consistency of the results.

2.5. Pore-Scale Visualization Experiments. The two-dimensional (2D) etched glass micromodel used for this research has a pattern similar to that used in previous research.[21,29] The micromodel

https://doi.org/10.1021/acs.energyfuels.3c00136
Energy Fuels 2023, 37, 5114−5129

Table 3. Nanomaterials' Details[a]

nanoparticle types	suppliers	SSA (m^2/g)	density (g/cm^3)	size	purity
short MWCNTs	Chengdu Organic Chemicals	350	2.1	8 nm OD, 2−5 nm ID, length (0.5−2 μm)	>98%
silicon dioxide (SiO_2) nanopowder	US Research Nanomaterials	170−200	2.4	15−20 nm	>99.5%
aluminum oxide (Al_2O_3) nanopowder	Sky-Spring nanomaterials	38	3.9	20 nm	>99%

[a]Notes: MWCNT, multiwalled carbon nanotubes; SSA, specific surface area.

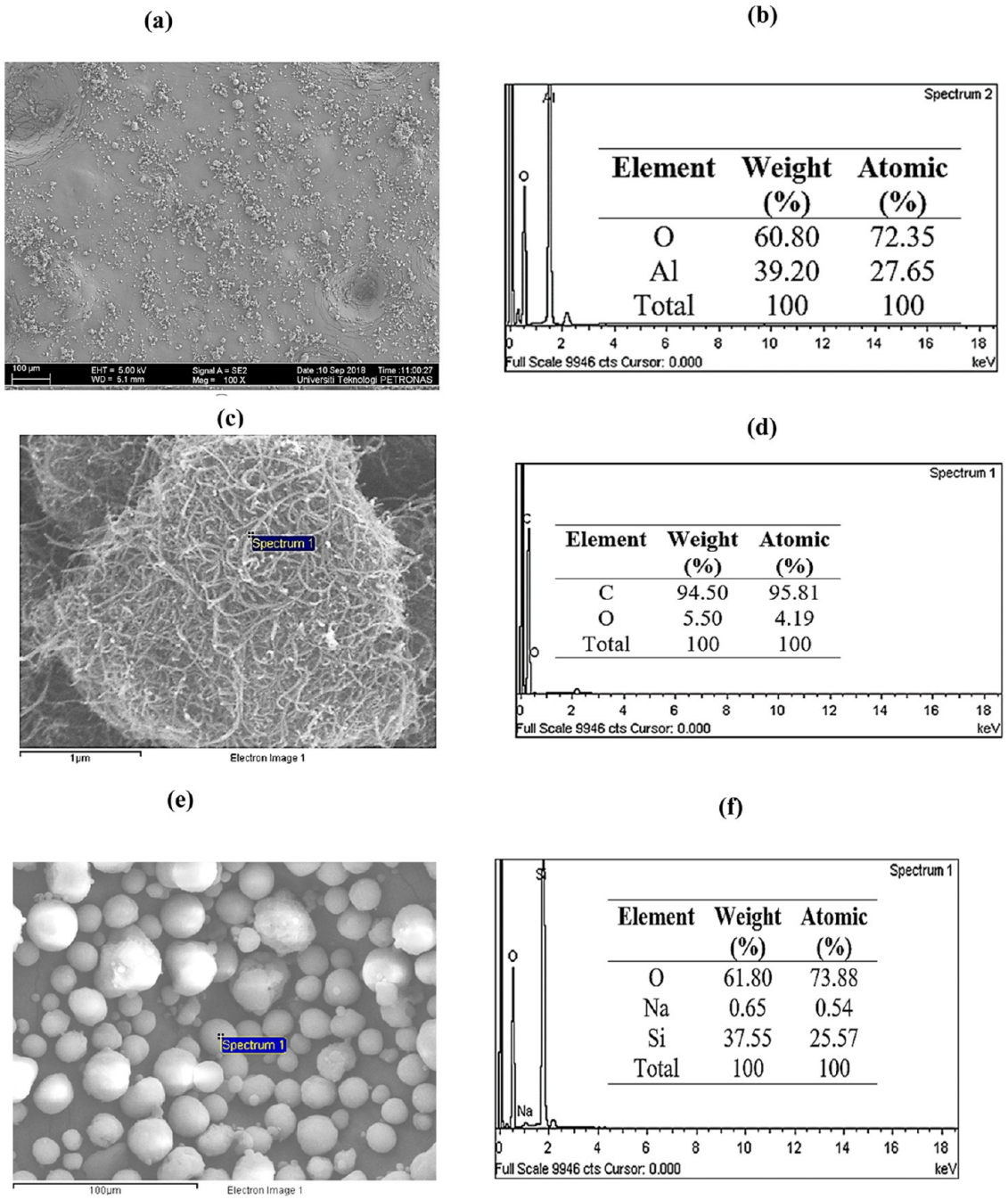

Figure 1. (a, b) Field-emission scanning electron microscopy (FESEM) images and energy-dispersive X-ray (EDX) analysis for Al_2O_3 nanoparticles. (c, d) Multiwalled carbon nanotubes. (e, f) SiO_2 nanoparticles.

Table 4. X-ray Fluorescence Analysis Results: Main Compositions of the Rock Substrate

SiO_2	Al_2O_3	Fe_2O_3	MgO	CaO	Na_2O	K_2O	TiO_2	P_2O_5	MnO	LOI
54.23	20.23	5.93	3.50	2.68	1.40	7.10	1.20	0.22	0.08	30

https://doi.org/10.1021/acs.energyfuels.3c00136
Energy Fuels 2023, 37, 5114−5129

was designed with mean pore sizes of about 600 μm and mean pore throats of about 300 μm. First, the patterns of the pore throats and bodies were sketched, and pore networks were etched onto the glass surface. The etched plate was then covered with another blank glass plate in an oven at 983.15 K. The micromodel was quite heterogeneous; hence, its permeability and porosity were estimated as 0.7 Darcy and 30%, respectively, using ImageJ software. Figure 2 depicts the micromodel when fully saturated with oil.

Figure 2. Oil-saturated 2D etched glass micromodel for pore-scale visualization experiments.

The micromodel was positioned horizontally to prevent the effects of gravity on fluid flooding. The brine and NPS emulsions were injected into the micromodel with NE-1000 syringe pumps. The initial connate water saturation was simulated by injecting a 3 wt % NaCl solution until the micromodel became fully saturated. This step was followed by the gradual injection of many pore volumes of crude oil. Afterward, NPS fluid emulsion flooding was conducted at 0.0017 mL/min. Pictures of the micromodel were taken every 1 h during fluid injection, and ImageJ software was used to calculate the trapped oil from the microscopic images. After every run, toluene and acetone were used to clean the micromodel and remove any trapped impurities.

2.6. Computational Fluid Dynamics Evaluation. The porous media geometries were modeled with Ansys 2021 R2 (Fluent Inc.) CFD software. Three designs were used, and the second design was like the pattern used for the pore-scale visualization experiments to compare the results of the simulation predictions with the results of the experimental studies and validate them. The first design had dimensions of 4.5 × 14 cm and a porosity of 40%, whereas the second and third designs have identical dimensions of 6 × 6 cm and porosity values of 34 and 35%, respectively (Table 4). Similar design patterns were used by Gharibshahi et al.[49] in a previous study.

The porous patterns in Model A were randomly distributed using the programming developed in C++ to maintain a constant porosity (40%). Nearly 1.7×10^5, 2.1×10^5, and 3.5×10^5 computational cells were employed to ensure that the three micromodels were divided into discrete control volumes. The designs were created in Design Modeler and automatically saved in the ANSYS Workbench for further preprocessing processes and mesh generation. Other simulation processes, such as equations solving and postprocessing, were accomplished in ANSYS Fluent. The porous patterns of the micromodels used for the CFD simulation are presented in Figure 3.

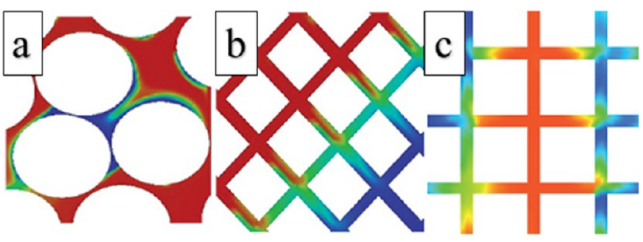

Figure 3. Porous patterns of the micromodels used for this research.

Kozeny–Carman[50,51] (eq 1) was used to compute the average radius of the pore throat for each micromodel design

$$r = \sqrt{\frac{8k}{\phi}} \tag{1}$$

where ϕ denotes the porosity, r represents the average pore throat radius (μm), and K indicates the permeability (10^{-10} μm^2). The calculation and measurement results are listed in Table 5.

Table 5. Porosity, Permeability, and Average Pore Throat Radius for Micromodel Designs

micromodel	porosity %	permeability (10^{-18} μm^2)	ave. pore throat radius μm
A	40.00	6.46	12.4568
B	34.83	1.12	4.3288
C	35.00	3.11	8.6829

Each grid was solved for the governing equation for the displacement fluid flow rate of 0.0006 cm^3/min and t = 0.01 s. The effects of time steps on the reliability of the results were assessed by conducting several tests at varying time intervals, and t = 0.01 s was eventually chosen for simulation predictions to minimize the simulation time and computational cost. The simulations were terminated when the steady-state condition was reached (i.e., when oil production from the micromodel stopped). Nodes 33447, 127450, and 243984 were the grids selected for Micromodels A–C. The number of computations was reduced by choosing grids with larger mesh sizes and fewer nodes.

The governing equations were solved using a simplified multiphase model (a mixture model). This model has been applied in previous studies to model the flow of a solid–liquid mixture through porous media by solving the energy, continuity, and momentum equations for the mixture.[43,44,52−54] The secondary phase volume fraction equation was used for NPS solutions, and algebraic expressions were used for the relative velocities.[43,55]

The fluid flow in porous media was investigated by solving the mass and momentum transport equation based on the finite volume approach using Fluent software. For the conservation of mass and conservation of momentum, respectively

$$\frac{\partial}{\partial t}(\rho_m) + \nabla\cdot(\rho_m \vec{V}_m) = 0 \tag{2}$$

$$\frac{\partial}{\partial t}(\rho_m \vec{v}) + \nabla\cdot(\rho_m \vec{v}_m \vec{v}_m) = -\nabla P_m + \nabla\cdot(\mu_m \nabla \vec{V}_m) + \nabla\cdot\sum_{k=1}^{n} \varphi_k \rho_k \vec{V}_{dr,k} \vec{V}_{dr,k} \tag{3}$$

The volume fraction equation is expressed as follows

$$\frac{\partial}{\partial t}(\varphi_p \rho_p) + \nabla\cdot(\varphi_p \rho_p \vec{V}_m) = -\nabla\cdot(\varphi_p \rho_p \vec{V}_{dr,p}) \tag{4}$$

Further, the energy equations are as follows

$$\frac{\partial}{\partial t}(\alpha_k \rho_k \vec{V}_m) + \frac{\partial \rho}{\partial t} + \nabla\cdot(\rho u) = 0$$

$$\frac{\partial(\rho u)}{\partial t} + u\cdot\nabla\cdot(\rho u) = \vec{V}_p - \vec{V}_f$$

$$\frac{\partial}{\partial}(\rho E) + \nabla\cdot(\vec{u}(\rho E + P)) = \nabla\cdot\left(k_{eff}\nabla T - \sum_i h_j \vec{J}_f + (\vec{J}_f\cdot\vec{u})\right)$$

$$\frac{\partial}{\partial t}((\alpha_k \rho_k \vec{V}_m) + \nabla\cdot\sum_{k=1}^{n}(\alpha_k \vec{V}_k \rho_k E_k + \rho) = \nabla\cdot(K_{eff}\nabla T) + S_E \tag{5}$$

https://doi.org/10.1021/acs.energyfuels.3c00136
Energy Fuels 2023, 37, 5114−5129

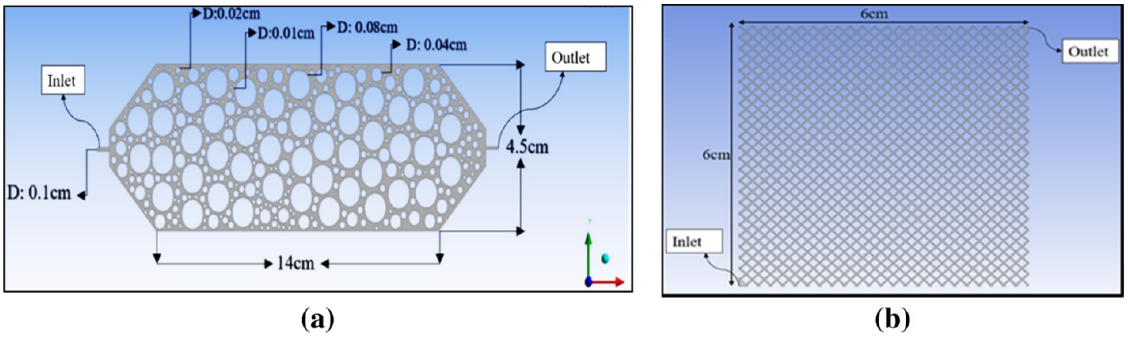

Figure 4. Dimension and boundaries of (a) model A and (b) model B.

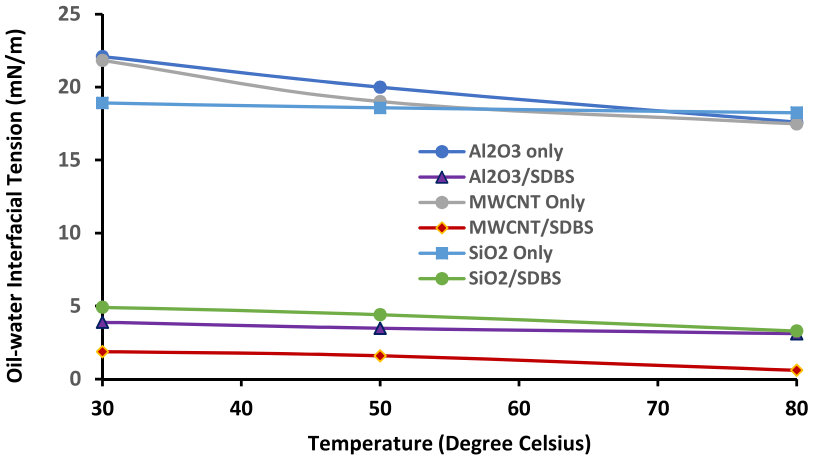

Figure 5. Nanofluid and nanoparticle-surfactant solution effects on decane-oil−water interfacial tension at various temperatures (prepared with 0.1 wt % nanoparticles and 0.1 wt % sodium dodecyl benzene sulfonate).

Moreover, NPS mixture properties are evaluated using eqs 6−8 for mixture viscosity, mixture density, and mixture velocity, respectively

$$\mu_m = \sum_{k=1}^{n} \varphi_k \mu_k \tag{6}$$

$$\rho_m = \sum_{k=1}^{n} \varphi_k \rho_k \tag{7}$$

$$\vec{V}_m = \frac{\sum_{k=1}^{n} \varphi_k \rho_k \vec{V}_k}{\rho_m} \tag{8}$$

The kth phase drift velocity (i.e., the kth phase velocity relative to the mixture velocity) is defined as follows

$$\vec{V}_{dr,k} = \vec{V}_k - \vec{V}_m \tag{9}$$

The slip velocity (relative velocity) can be described as the secondary phase (NPS) velocity (P) relative to the primary phase (oil) velocity (f) with the following expression

$$\vec{V}_{Pf} = \vec{V}_P - \vec{V}_f \tag{10}$$

The relationship between the relative velocity and drift velocity can be expressed as follows

$$\vec{V}_{dr,k} = \vec{V}_{Pf} - \sum_{k=1}^{n} \frac{\varphi_k \rho_k}{\rho_{eff}} \vec{V}_{fk} \tag{11}$$

The input parameters for the simulation include the viscosity and density of the crude oil and the displacing fluid (nanofluids or NPS solutions) and the IFTs between the oil and displacing fluids at various experimentally determined conditions. The input velocity at the inlet is 0.000129 m/s. The micromodels are designed with different geometries but with the same size of the inlet and outlet. The dimensions and boundaries of micromodels A and B are presented in Figure 4; micromodels B and C have the same dimensions and boundaries.

The following are the relevant assumptions in the mixture model development.

1. The velocity outlet was chosen as the outlet port.
2. The wall boundary conditions were assumed, suggesting that no entering or exit of flow occurs from the other edges.
3. The flow is a two-phase flow.
4. The secondary phase is water, surfactant fluid, or NPS slugs, whereas the primary phase is oil.
5. The initial saturation of the water is zero (S_{wi} = 0), and the injected water is distilled.
6. The development is in the transient state condition.
7. All simulation runs were conducted at the time interval of t = 0.01 s.
8. Iteration processes were carried out for 10,000 s until the oil production remained constant to establish a decent evaluation comparison of the models.
9. Gravity was not accounted for in the governing equations due to the low thickness of and horizontal positioning of the micromodel.

3. RESULTS AND DISCUSSION

This section discusses the results of the IFT and contact angle experiments, pore-scale visualization, and CFD simulation predictions.

3.1. Nanofluid and Nanosurfactant Solution Effects on Oil−Water Interfacial Tension. We measured the oil−water IFTs and contact angles to assess the influence of various

https://doi.org/10.1021/acs.energyfuels.3c00136
Energy Fuels 2023, 37, 5114−5129

NPS solutions on reducing the IFT and contact angle. The decane-oil−water IFT presented in Figure 5 suggests that an ultralow IFT was not obtained at any temperature with the three investigated nanomaterials. However, the IFT of the decane-oil−water was reduced significantly by NPS solutions compared to only nanofluids. In addition, the lowest IFT was demonstrated by MWCNT/SDBS when contrasted with the Al_2O_3/SDBS and SiO_2/SDBS solutions. The system energy is minimized by the adsorption of nanofluids on the oil−water interface, resulting in significant reduction in IFT.[10]

For instance, at room temperature (30 °C), the decane-oil−water IFT decreased from 48.010 to 21.827 mN/m using the MWCNT nanofluid, and it was considerably reduced to 2.618 mN/m with the MWCNT/SDBS solution. However, at similar conditions, the Al_2O_3/SDBS and SiO_2/SDBS solutions could only reduce the IFTs to 8.169 and 9.197 mN/m, respectively. These results suggest that, compared to other nanoparticle/surfactant solutions, the MWCNT/SDBS flow should effectively remove the trapped oil in the 2D etched glass micromodel pore walls and throats, increasing the oil recovery. The lower IFT between the injected fluid and resident oil facilitates easier oil displacement and mobilization and the separation of oil from the pore walls and channels.[56,57]

These results are in line with previous studies; results of previous research have shown significant reduction in IFT between the oil phase and the water phase due to the presence of plate-shaped nanoparticles at the interface, suggesting that nanosheets/nanoparticles are surface-active agents,[58] and their surface activity increased in the presence of surfactants. The modification of nanoparticle surfaces with surfactants significantly improved the dispersity of the nanofluids. The repulsion between the negatively charged SDBS molecules bonded onto negatively charged SiO_2 nanoparticle surfaces also reduced the nanoparticle agglomerations. The oil−water IFT was significantly higher when the nanofluids were dispersed in aqueous solutions compared to when the nanofluids were dispersed in surfactant solutions because of poor dispersion of nanoparticles in water.

Oil recovery by NPS solutions could result from adsorbing NPS solutions onto pore surfaces and alteration of the porous medium wettability from oil-wet to water-wet. The contact angles for the nanofluid/NPS solutions were measured to evaluate the suitability of the NPS solutions for altering the porous medium wettability compared to the nanofluid solutions. Figures 6 and 7 indicate that the contact angles changed slightly from 68.5° with the MWCNT, Al_2O_3, and SiO_2 nanofluids.

However, the contact angle decreased significantly in the presence of NPS solutions. The introduction of the MWCNT/SDBS droplet onto the rock surface demonstrated the lowest contact angle (20.1°); the introduction of Al_2O_3/SDBS and SiO_2/SDBS droplets reduced the contact angles to 26.02 and 25.41°, respectively. The contact angle data sets revealed that the adsorption of NPS solutions onto the pore surfaces during nanoparticle-surface flooding could significantly alter the porous medium wettability. The order of decreasing contact angles for NPS solutions is MWCNT/SDBS < SiO_2/SDBS < Al_2O_3/SDBS, suggesting that the alteration in porous media wettability for MWCNT/SDBS dispersion was the most significant.

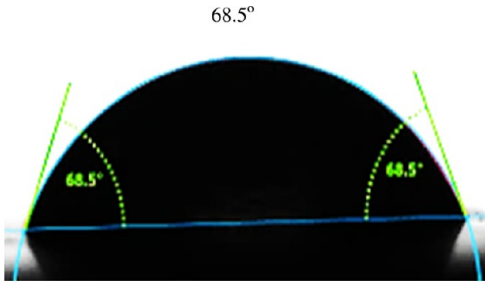

Figure 6. Sessile droplet images of water droplets on rock surfaces (68.5°).

An equilibrium exists between the solid−liquid IFT (γ_{sl}), liquid−gas IFT (γ_{lg}), and solid−gas IFT (γ_{sg}), as the water droplet was placed on the rock surface during the contact angle measurement, as indicated in the following equation[34,59]

$$\gamma_{sg} = \cos\theta_c\gamma_{lg} + \gamma_{sl} \quad (12)$$

The results of previous studies demonstrated that solid−liquid IFT (γ_{sl}) plays a prominent role when contact angle measurement is conducted with the sessile drop technique. In addition, the contact angle between the glass surface and liquid droplets is smaller at a higher γ_{sl} value.[34,59−61] Hydrogen bonds could be formed between the surface agents (the surfactant and nanomaterials) and water molecules. The formation of a hydrogen bond increases γ_{sl}; thus, the contact angle reduces when the NPS solution droplets are placed on rock surfaces. The main rock composition in this research is SiO_2 (54°). Therefore, hydrogen-bond formation is possible between the surface-active complex (nanoparticles and surfactant) and the rock structure, which can augment the surface energy and increase the hydrophilicity of the rock surface.

3.2. Pore-Scale Visualization Experiments. The pore-scale visualization experiments were conducted at an ambient temperature and pressure to assess the interaction between the NPS emulsion and resident crude oil in the 2D etched glass micromodel. The microscopic images at 1 and 5 h during the NPS flooding processes are presented in Figures 8−10. The effectiveness of various NPS emulsions in mobilizing trapped oil was evaluated from the oil retained within each micromodel after 5 h of NPS solution flooding.

The ImageJ analysis of the microscopic pictures at different time intervals revealed that the lowest amount of oil was retained within the micromodel when it was flooded with carbon nanotube-surfactant solutions (37.84%). The oil retained within the micromodel after Al_2O_3-SDBS and SiO_2-SDBS flooding was 58.48 and 43.42%, respectively. A lower quantity of oil was retained in the model during carbon nanotube-surfactant solution flooding, confirming that nanotube-surfactant solutions could be more effective for oil recovery than Al_2O_3 and SiO_2 surfactant solutions. The fluid flow patterns also indicated that oil displacement with carbon nanotubes and SiO_2 particles was more uniform and piston-like than displacement with Al_2O_3/surfactant flooding.

This observation agrees with the results of previous research.[30,35] Improvement in oil displacement efficiency during carbon-nanotube/surfactant emulsion flow has been attributed to the orientation of the cylindrical carbon nanotubes at the oil−water interface.[29−31] The NPS solutions interact with the resident oil to form stable in situ emulsions, which further assist in mobilizing and unlocking the oil trapped in pore spaces and throats. Moreover, the IFT and contact angle data sets discussed in Section 3.1 exhibited a significant

https://doi.org/10.1021/acs.energyfuels.3c00136
Energy Fuels 2023, 37, 5114−5129

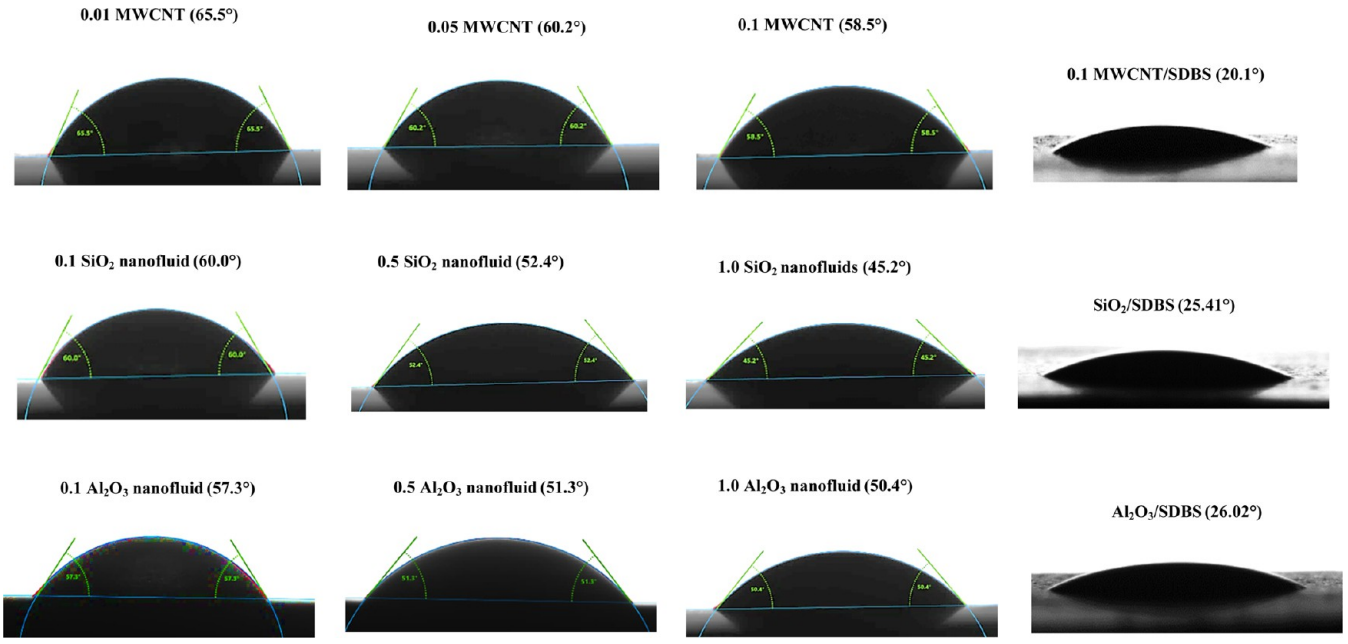

Figure 7. Sessile droplet images of nanofluids and nanoparticle-surfactant solutions on rock surfaces (prepared with 0.1 wt % nanoparticles and 0.1 wt % sodium dodecyl benzene sulfonate).

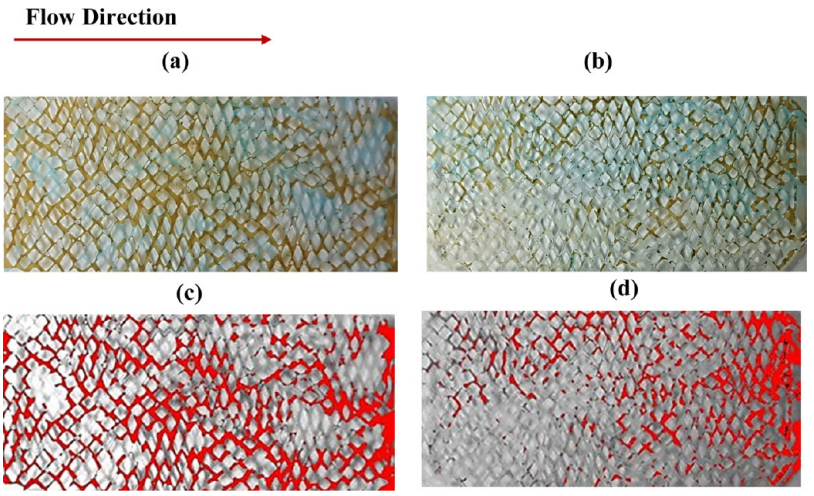

Figure 8. Microscopic images of the emulsion solution flow of SiO_2-sodium dodecyl benzene sulfonate within the 2D etched glass micromodel after (a) 1 h and (b) 5 h, and the residual oil determination by ImageJ after (c) 1 h and (d) 5 h. Crude oil is brownish in (a) and (b) and red in (c) and (d).

alteration of the porous media wettability into a more hydrophilic state and reduced the oil−water IFT in NPS solutions. This process contributed to the EOR potential of NPS solutions. The pore-scale visualization experiments provide insights into the process of detachment of the trapped oil droplet, confirming the impact of rock wettability alteration and reduction of IFT between water phase and oil phase on eventual oil recovery.

3.3. Computation Fluid Dynamic Simulation Results. The CFD simulation predictions were conducted to assess the EOR effectiveness of different NPS fluids at various temperatures and low flow rates representative of downhole conditions and to identify the prevailing EOR mechanisms for mobilizing the resident oil using the displacing fluids. The effect of pore geometry was also considered.

3.3.1. Influence of Temperature on Hydrocarbon Recovery by the Injected Fluids. Two temperature conditions (30 and 80 °C) were considered to assess the influence of temperature on the performance of various injection fluids. In addition, NPS fluid injections were conducted to mimic the injection of NPS slugs into an oil-filled porous media, whereas the brine and surfactant solution injections were conducted to simulate water-flooding and surfactant-injection scenarios. The oil recovery factors at various temperatures for different displacing fluids are depicted in Figures 11−13. The CFD simulation results for the two modeled temperature cases revealed that the trapped oil saturation was higher at high temperatures.

Similarly, a comparison of the final oil recovery corresponding to the various cases of the NPS solution injections confirmed the results of the pore-scale visualization experiments: the synergy of MWCNTs and surfactant solutions produces the highest oil recovery compared to Al_2O_3-SDBS and SiO_2-SDBS fluids. For instance, after 48 h, the oil recovery

https://doi.org/10.1021/acs.energyfuels.3c00136
Energy Fuels 2023, 37, 5114−5129

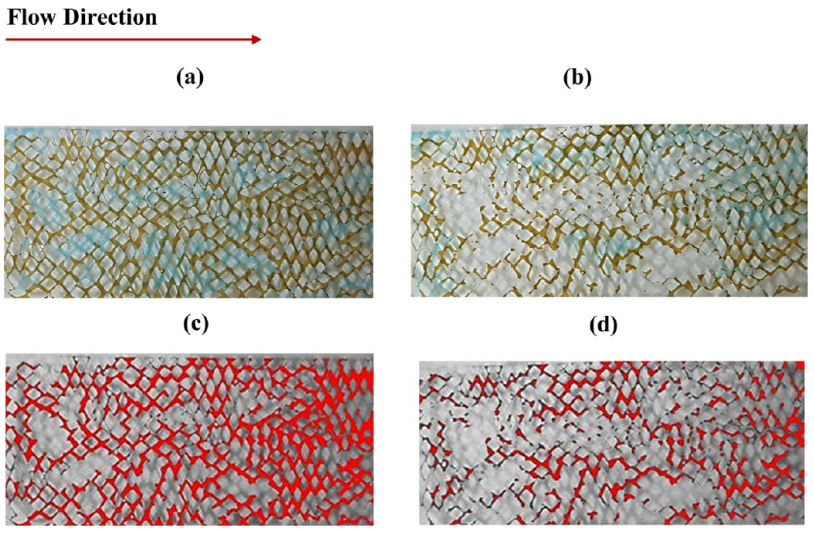

Figure 9. Microscopic images of the emulsion solution flow of Al_2O_3-sodium dodecyl benzene sulfonate within the 2D etched glass micromodel after (a) 1 h and (b) 5 h, and the residual oil determination by ImageJ after (c) 1 h and (d) 5 h. Crude oil is brownish in (a) and (b) and red in (c) and (d).

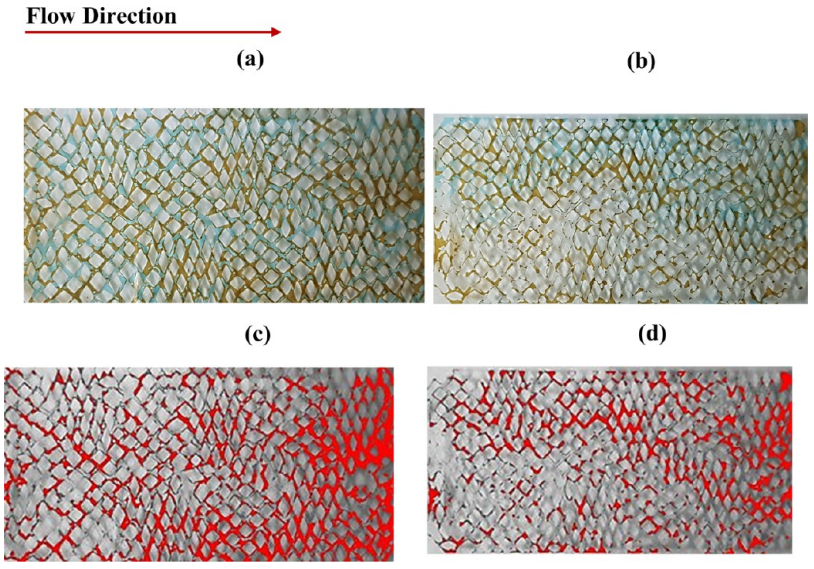

Figure 10. Microscopic images of the emulsion solution flow of multiwalled carbon nanotube-sodium dodecyl benzene sulfonate (SDBS) within the 2D etched glass micromodel after (a) 1 h and (b) 5 h, and the residual oil determination by ImageJ after (c) 1 h and (d) 5 h. Crude oil is brown in (a) and (b) and red in (c) and (d) (prepared with 1 wt % nanoparticles and 0.1 wt % SDBS).

factor from CFD simulations in Design A revealed that, at 30 °C, the percentage of oil recovered by the MWCNT-SDBS solution is 41.2%. In addition, SiO_2-SDBS and Al_2O_3-SDBS solutions recovered 38.7 and 33.5% of the trapped oil, respectively. However, the surfactant SDBS and water exhibited the lowest oil recovery factor of 22.45 and 10.2%, respectively.

Similarly, at 80 °C, the oil recovery factor via MWCNT-SDBS solution flooding is 34.4%, and SiO_2-SDBS and Al_2O_3-SDBS solutions have recovery factors of 30.3 and 28.1%, respectively, whereas SDBS and water-flooding have very low recovery factors of 17.54 and 8.9%, respectively.

Most previous investigations of the effects of temperature on oil recovery through CFD simulation in the literature were conducted for heavy oil.[44,56] Researchers have found that oil recovery is higher at high temperatures because the viscosity of the oil and oil−water IFT reduces at high temperatures. Moreover, the C−C bonds of resin and asphaltene contents of very heavy oil break at high temperatures through nanofluid injection.[44] Hence, increasing the injected fluid temperature permits more oil to exit the micromodel conveniently.

In this study, although lower oil−water IFT obtained at 80 °C is expected to facilitate easier displacement and oil detachment from pore walls and channels, the viscosity values of the oil for this research (0.94 cp for decane and 10 cp for crude oil) are quite low. Thus, the recovery factor did not increase with temperature but decreased at 80 °C. Moreover, the oil−water IFT only slightly reduced with increased temperature (Figure 5).

Figures 11−13 further confirmed that the order of increasing oil recovery factor with different injected fluids is MWCNT-SDBS > SiO_2-SDBS > Al_2O_3-SDBS > SDBS > water-flooding. These results agree with the pore-scale visualization experimental results. When the NPS emulsions were injected into

https://doi.org/10.1021/acs.energyfuels.3c00136
Energy Fuels 2023, 37, 5114−5129

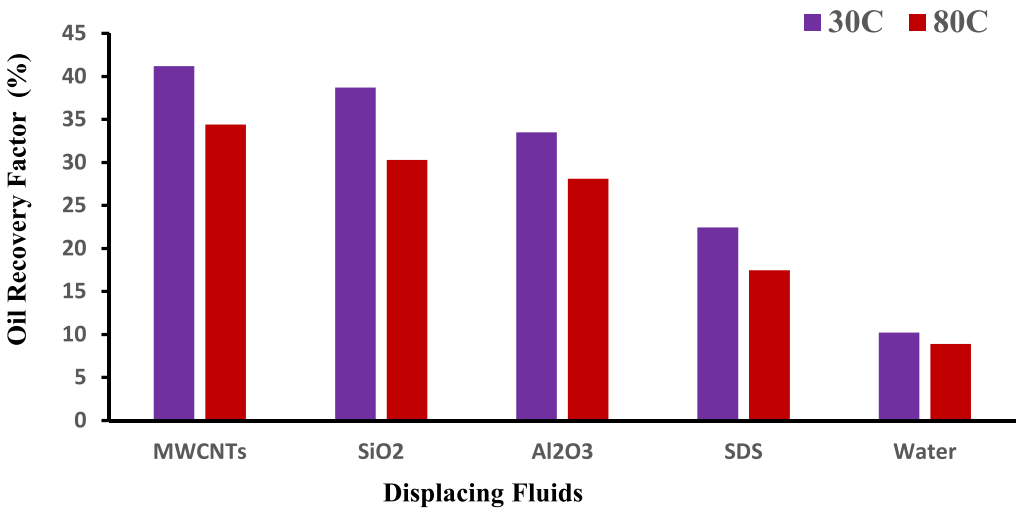

Figure 11. Effect of displacing fluids on the oil recovery factor at various temperatures for micromodel Design A (prepared with 0.1 wt % nanoparticles and 0.1 wt % sodium dodecyl benzene sulfonate).

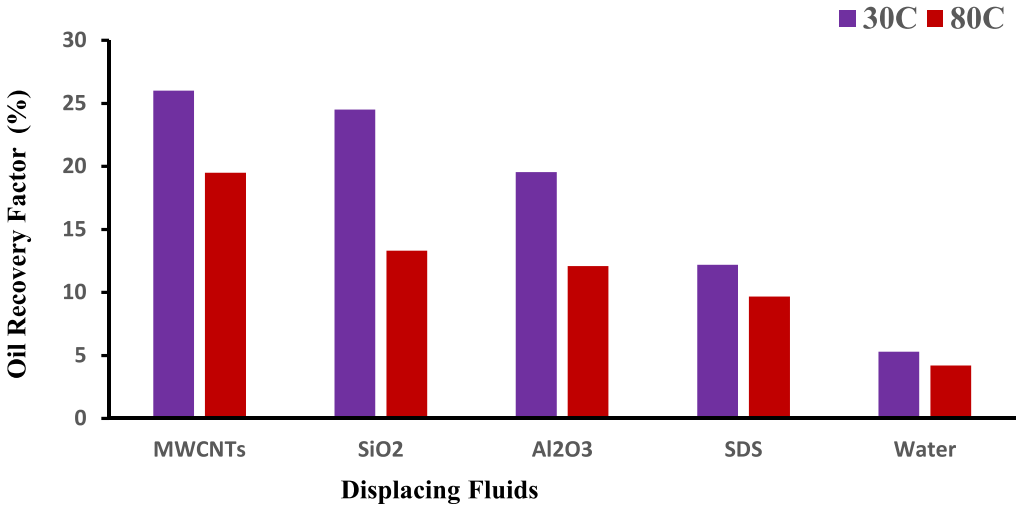

Figure 12. Effect of displacing fluids on the oil recovery factor at various temperatures for micromodel Design B (prepared with 0.1 wt % nanoparticles and 0.1 wt % sodium dodecyl benzene sulfonate).

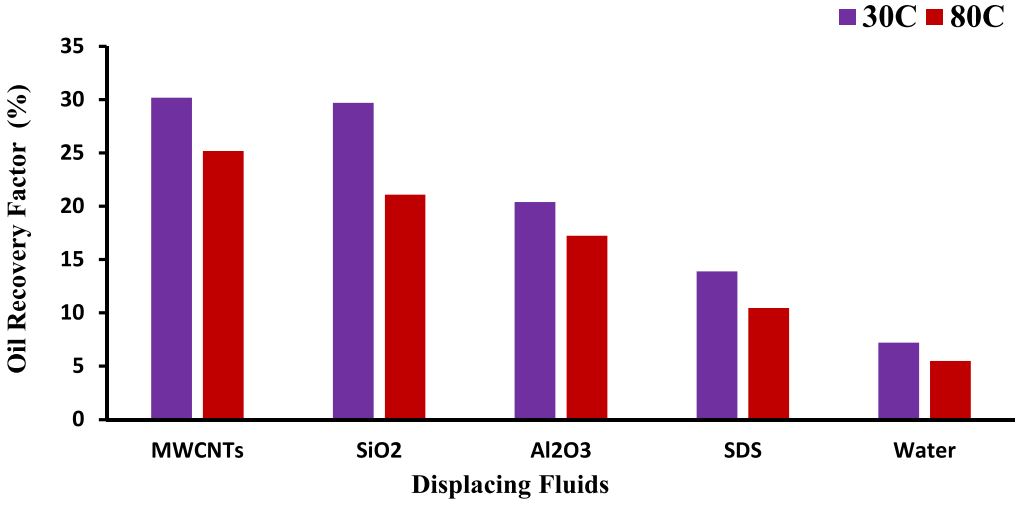

Figure 13. Effect of displacing fluids on the oil recovery factor at various temperatures for micromodel Design C (prepared with 0.1 wt % nanoparticles and 0.1 wt % sodium dodecyl benzene sulfonate).

https://doi.org/10.1021/acs.energyfuels.3c00136
Energy Fuels 2023, 37, 5114−5129

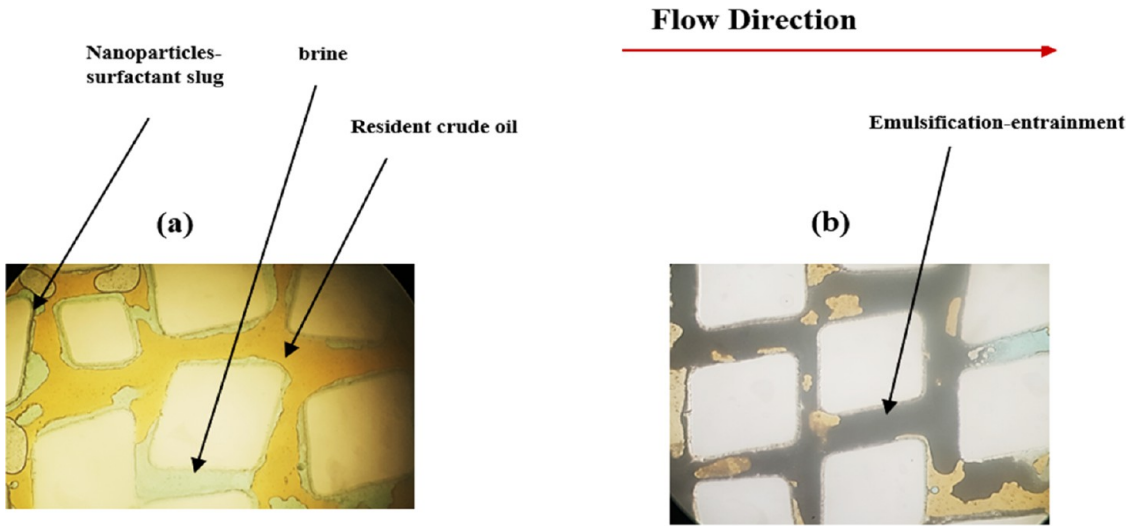

Figure 14. Pore-scale visualization of the nanoparticle-surfactant emulsion flow in the 2D etched glass micromodel displaying emulsification entrainment.

crude oil-filled etched glass micromodels, it was very easy to distinguish all phases in the micromodel at the onset of NPS flooding (Figure 14). For easy identification, the oil is yellow, the water is blue, and the NPS emulsion slug is white (Figure 14a).

However, the solution mixed with the resident crude oil over time, resulting in the formation of an in situ emulsion. Thus, a black liquid was formed as the NPS slug interacted with the resident oil, confirming the emulsification entrainment phenomenon (Figure 14b). Similar observations have been reported in previous research.[62−64] The residual oil to be mobilized by the NPS solution is emulsified and entrained into the flowing NPS solutions to form a more stable and continuous front serving as a secondary displacing fluid for the oil locked in the rock pores.

3.3.2. Fingering, Channeling, and Trapping Effects. The microscopic images from the CFD (Figure 15) agreed with the experimental results regarding fingering, channeling, and trapping effects in the flow patterns of MWCNT-SDBS, SiO_2-SDBS, and Al_2O_3-SDBS solutions. However, these effects were less severe during the MWCNT-SDBS flow process than in the other NPS fluids. The CFD microscopic images further suggest that the volume of trapped oil in the porous media was higher after SiO_2-SDBS and Al_2O_3-SDBS dispersion flooding than after MWCNT-SDBS solution flooding.

A comparison of the NPS solutions' flow with SDBS injection and water-flooding indicated that the displacement front of the NPS dispersions was finer, and the mobility was lower than the SDBS solution and water-flooding. This can be attributed to the formation of a thick film on the pore walls and channels of the porous media during NPS solution flows, as observed in Figure 14. However, the displacing fluid front was in the form of a ganglion via the higher permeability layer during the pure surfactant (SDBS) and water-flooding, resulting in significant trapping of a high quantity of oil in the pores.

These CFD microscopic results (Figure 15) agreed with the computed oil recovery factor presented in Figures 11−13, confirming that the injection of NPS solutions can cause significant mobilization of the oil trapped in the thin pore throats and microchannels of the reservoir rock than could ever be achieved through only surfactant solution injection or water injection. The finer displacement front and lower mobility of NPS assisted in residual oil mobilization. Moreover, the NPS active complex exhibited a high predisposition to reduce the oil−water IFT and altered the rock-wetting tendency to more hydrophilic conditions, making it easier for the oil droplets to be easily stripped from the rock surfaces. Moreover, the NPS active complex is tightly packed at the oil−water interface to form a fairly stable interfacial film, which is favorable for oil displacement.

In the absence of nanoparticles (SiO_2, Al_2O_3, and MWCNTs), the fingering phenomenon was more significant, and the injected fluid could not properly sweep the oil in the micromodel. However, during NPS solution flooding, a piston-like behavior was demonstrated due to decreasing oil−water IFT, attainment of a more water-wet state, and the decreasing mobility of the injected fluid. The porous medium becomes more water-wet, resulting in an enhanced detachment of the oil layer from the wall of the porous space. Thus, the fingering phenomenon was less severe because the displacing fluids could overcome the capillary pressure in the pore throats and bodies.

Generally, the MWCNT-SDBS solutions demonstrated the lowest oil−water IFT and contact angles, the highest oil recovery, and the finest displacement front compared to other NPS solutions, SDBS solution dispersions, and water-flooding. Moreover, the water-flooding and sole SDBS-surfactant flooding displayed the lowest oil recovery potentials at high temperatures due to the considerable channeling and fingering of the injected fluid through high-permeability layers compared to NPS fluids (Figures S1−S3 in the Supporting Information).

3.3.3. Heterogeneity Effect. The CFD simulations can assess the influence of porous media heterogeneity on hydrocarbon recovery via NPS solution flooding by designing three models with varied pore sizes, pore-to-throat connectivity, and random pore distribution. The simulation predictions from this model represent a two-phase flow at the actual reservoir conditions and permit an appropriate observation of the injected fluid front and fingering, channeling, and trapping effects during residual oil mobilization.[49] The comparison of the microscopic images from the

https://doi.org/10.1021/acs.energyfuels.3c00136
Energy Fuels 2023, 37, 5114−5129

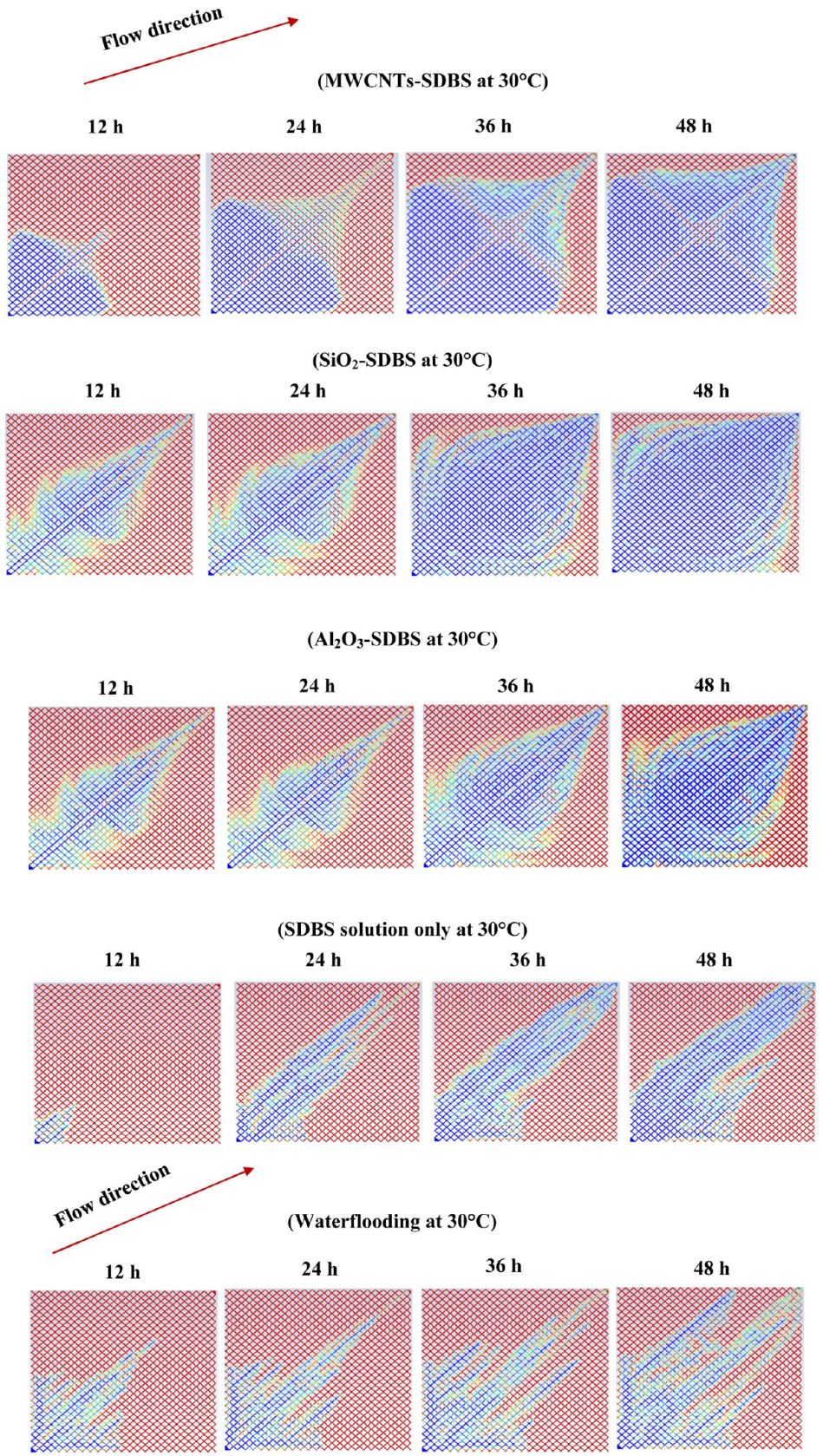

Figure 15. Computational fluid dynamic microscopic images of the displacing fluid front at different times (prepared with 0.1 wt % nanoparticles and 0.1 wt % sodium dodecyl benzene sulfonate). The displacing fluid is blue; the displaced fluid (oil) is red.

three models demonstrated that porous media heterogeneity plays a prominent role in influencing oil recovery, residual oil mobilization, and displacement from porous media (Figures S1−S3 in the Supporting Information).

https://doi.org/10.1021/acs.energyfuels.3c00136
Energy Fuels 2023, 37, 5114−5129

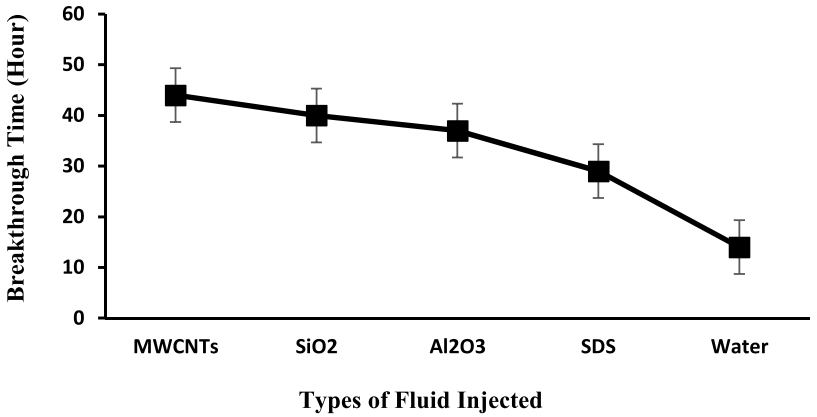

Figure 16. Breakthrough time for injected fluids at 30 °C for Design B (prepared with 0.1 wt % nanoparticles and 0.1 wt % sodium dodecyl benzene sulfonate).

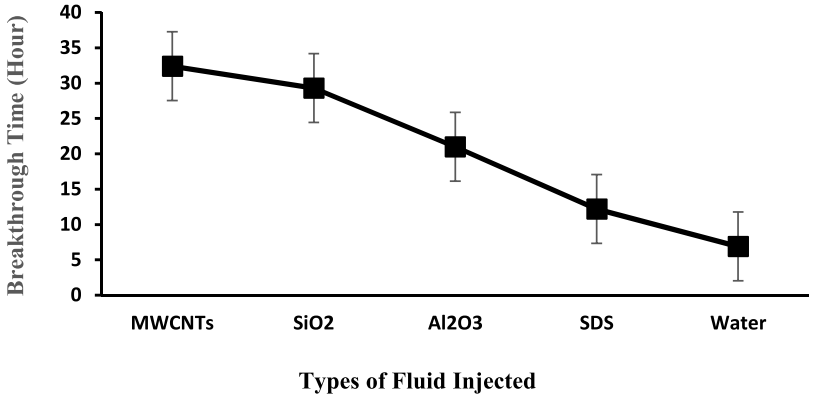

Figure 17. Breakthrough time for injected fluids at 80 °C for Design B (prepared with 0.1 wt % nanoparticles and 0.1 wt % sodium dodecyl benzene sulfonate).

For all injected fluids, the fingering effect was more severe in Model B, with a more complex geometry than in Models A and C. Some tortuosity effects were introduced into Model B, ensuring that the flow directions of the displacing fluids are not straightforward like those of Models A and C, and the flow direction of the injected fluid is not the same as the pore body to pore throat connections. Compared to Model B, the flow is regular in Models A and C, and the sweeping front of the injected fluid is uniform (piston-like), resulting in a higher oil recovery factor and macroscopic sweep efficiency. Due to the tortuosity of Model B, the injected fluid could not effectively overcome the capillary pressure in the pore throats and bodies, resulting in poor sweep efficiency and lower oil recovery factors (Figure 12).

The design of Model B is similar to the micromodel used for the experimental sections and the design used by Gharibshahi et al.[49] The macroscopic images of Models A−C presented in Figures S1−S3 further confirm that the order of EOR by the displacing fluids is MWCNT-SDBS > SiO_2-SDBS > Al_2O_3-SDBS > SDBS > water-flooding. The tortuosity pattern introduced into Model B intensified the heterogeneity effects during surfactant and water-flooding, resulting in unfavorable water channeling, as well as poor water and surfactant circulations in the porous medium and low sweep efficiency.

3.3.4. Influence of Breakthrough Time on Residual Oil Mobilization. The observation of the flow phenomenon and injected fluid front from the CFD microscopic images indicated that the order of decreasing breakthrough time for the injected fluid is water injection < SDBS solution flooding < Al_2O_3-SDBS < SiO_2-SDBS < MWCNT-SDBS (Figures 16 and 17). The faster breakthrough of the water and SDBS solution compared to NPS fluids in Models B and C is because the injected fluids could not effectively overcome the capillary pressure in the pores and throats. Due to the pore geometry and model tortuosity, the displacing fluid advancing fronts (water and SDBS solution) cannot sweep and unlock the trapped oil in portions not along its path. In such cases, the breakthrough time is faster, as the injected fluid only mobilizes the resident oil along its path, leaving a high quantity of trapped oil immobilized in porous media. Thus, the mobility of the injected fluid was very high, and the macroscopic sweep efficiency was lower than that of the NPS solutions.

The lower mobility of the Al_2O_3-SDBS, SiO_2-SDBS, and MWCNT-SDBS fluids delayed the injected fluid mobility and the residence time, promoting the migration of the injected fluid front into other portions that were not along the injection path and zones of lower permeability. Thus, the breakthrough time was higher, and the macroscopic sweep efficiency and oil recovery factor were higher (Figures 16 and 17).

At realistic reservoir conditions, the fluid flow phenomenon is not as straightforward as portrayed in several unconsolidated porous media designs. Pore heterogeneity and tortuosity usually compel the displacing fluids to change flow paths and directions.[65] When the diameter of the pore throats and bodies is larger and less tortuous, it permits an easier fluid flow from the inlet to the outlet, and the recovery factor from such a

https://doi.org/10.1021/acs.energyfuels.3c00136
Energy Fuels 2023, 37, 5114−5129

model is higher compared to models with smaller and more complex pore throats and bodies (Figures 10–12).

When the level of tortuosity and heterogeneity is very high, the injected fluid cannot overcome the capillary pressure of the trapped oil to mobilize the oil.[34,66] The lowest oil recovery factor was achieved with Model A because the micromodel design is not complex, the pore throats and bodies are less tortuous, and circles are distributed randomly, allowing the fluid to flow easily.

4. CONCLUSIONS

In this research, we conducted pore-scale visualization experiments and CFD simulations to assess the synergistic influence of SDBS and various nanomaterials (MWCNTs, Al_2O_3, and SiO_2 nanoparticles) on EOR from 2D etched glass micromodels. Ansys 2021 R2 (Fluent Inc) CFD software created micromodels with three patterns and pore geometries. The fluid flow in porous media was investigated by solving the mass and momentum transport equation based on the finite volume approach using Fluent software. Changes in contact angles of the displacing fluid droplets on rock surfaces and oil–water IFT for various NPS fluids were measured to explain the results of the microscopic experiments and elucidate the EOR mechanisms. The following are the main conclusions from the research results.

- The addition of nanoparticles to SDBS solutions significantly increased the oil recovery factor and displacement fluid breakthrough time and decreased the fingering and channeling effects, producing a more uniform and symmetric flow with a finer displacing front than for water injection and solely SDBS flooding.
- The order of the increasing oil recovery factor and breakthrough time was MWCNT/SDBS > SiO_2/SDBS > Al_2O_3/SDBS > SDBS > water-flooding. This result was attributed to the orientation of the MWCNT/SDBS active complex at the solid–liquid and liquid–liquid interfaces, the lower oil–water IFT, and the contact angles achieved by the NPS solutions.
- The oil recovery factor decreased, whereas the fingering effect generally increased when the pore distribution was randomly generated and less tortuous, suggesting that low oil recovery should be expected in realistic fluid flow conditions in heterogeneous reservoirs compared to unconsolidated homogeneous porous media.
- Although the oil–water IFT values were lower at high temperatures, the oil recovery factor decreased with increasing temperatures, indicating that the temperature effect on enhancing the oil recovery via breaking of carbon–carbon bond resin and the asphaltene content of crude oil is only significant when the viscosity of the oil is very high.
- The CFD approach provides opportunities to stimulate the NPS fluid flow at realistic reservoir temperatures and flow conditions, generally producing lower oil recovery factors than the experimental results, suggesting that CFD is a versatile tool for a more accurate simulation of microscopic EOR mechanisms using NPS fluids.

ASSOCIATED CONTENT

Supporting Information

The Supporting Information is available free of charge at https://pubs.acs.org/doi/10.1021/acs.energyfuels.3c00136.

Fingering effects of the nanoparticle-surfactant solutions, and SDS flooding and water-flooding at 30 and 80 °C in models A–C (PDF)

AUTHOR INFORMATION

Corresponding Authors

Nurudeen Yekeen – *Department of Petroleum Engineering, Universiti Teknologi PETRONAS, Seri Iskandar 32610 Perak, Malaysia; School of Engineering, Edith Cowan University, Joondalup 6027 WA, Australia;* orcid.org/0000-0001-6738-7893; Email: peteryekeen@yahoo.com

Muhammad Ali – *Physical Science and Engineering Division, King Abdullah University of Science and Technology (KAUST), Thuwal 23955, Saudi Arabia;* orcid.org/0000-0002-2446-3072; Email: Muhammad.ali.2@kaust.edu.sa

Authors

Ali Masoud Ali Elakkari – *Department of Chemical & Petroleum Engineering, Faculty of Engineering, Technology and Built Environment, UCSI University, Kuala Lumpur 56000, Malaysia*

Javed Akbar Khan – *Institute of Hydrocarbon Recovery, Universiti Teknologi PETRONAS, Seri Iskandar 32610, Malaysia;* orcid.org/0000-0001-8399-2532

Ahmed Al-Yaseri – *Center of Integrative Petroleum Research (CIPR), College of Petroleum Engineering and Geoscience, King Fahd University of Petroleum and Minerals, Dhahran 31261, Saudi Arabia;* orcid.org/0000-0001-9094-1258

Hussein Hoteit – *Physical Science and Engineering Division, King Abdullah University of Science and Technology (KAUST), Thuwal 23955, Saudi Arabia;* orcid.org/0000-0002-3900-7272

Complete contact information is available at: https://pubs.acs.org/10.1021/acs.energyfuels.3c00136

Notes

The authors declare no competing financial interest.

ACKNOWLEDGMENTS

The authors acknowledge Luk Cox, a scientific illustrator from King Abdullah University of Science and Technology, Saudi Arabia, for producing the graphical abstract TOC.

NOMENCLATURE AND UNITS

$\vec{V}_{dr,k}$ = drift velocity of the kth phase, m/s
$\vec{V}_{dr,p}$ = drift velocity of a secondary phase, m/s
$\vec{V}_f$ = velocity of the primary phase, m/s
$\vec{V}_k$ = velocity of the kth phase, m/s
$\vec{V}_m$ = mixture velocity, m/s
$\vec{V}_p$ = velocity of the secondary phase, m/s
$\vec{V}_{pf}$ = slip velocity, m/s
Δt = time step, sec
μ_{bf} = viscosity of the base fluid, mPa s
μ_m = mixture viscosity, mPa s
μ_{nf} = viscosity of the nanofluid, mPa s
μ_p = viscosity of the secondary phase, mPa s
ρ_{bf} = density of the base fluid, kg/m^3
ρ_m = mixture density, kg/m^3
ρ_{nf} = density of the nanofluid, kg/m^3
ρ_p = density of the secondary phase, kg/m^3
dr = drift

https://doi.org/10.1021/acs.energyfuels.3c00136
Energy Fuels 2023, 37, 5114–5129

p = secondary phase
K = kth phase

REFERENCES

(1) Ahmad, T.; Zhang, D. A critical review of comparative global historical energy consumption and future demand: The story told so far. *Energy Rep.* **2020**, *6*, 1973−1991.
(2) Okundamiya, M. Size optimization of a hybrid photovoltaic/fuel cell grid connected power system including hydrogen storage. *Int. J. Hydrogen Energy* **2021**, *46*, 30539−30546.
(3) Jariah, N. F.; Hassan, M. A.; Taufiq-Yap, Y. H.; Roslan, A. M. Technological Advancement for Efficiency Enhancement of Biodiesel and Residual Glycerol Refining: A Mini Review. *Processes* **2021**, *9*, 1198.
(4) Tackie-Otoo, B. N.; Atta, D. Y.; Ayoub Mohammed, M. A.; Otchere, D. A. Investigation into the oil recovery process using an organic alkali−amino acid-based surfactant system. *Energy Fuels* **2021**, *35*, 11171−11192.
(5) Abo-Riya, M. A.; Baker, S. A. Novel synthesized anionic gemini and monomeric surfactants bearing sulphonate group as petro-dispersing/collecting agents: Design, characterization and surface-active properties. *J. Mol. Struct.* **2023**, *1274*, No. 134502.
(6) Yekeen, N.; Malik, A. A.; Idris, A. K.; Reepei, N. I.; Ganie, K. Foaming properties, wettability alteration and interfacial tension reduction by saponin extracted from soapnut (Sapindus Mukorossi) at room and reservoir conditions. *J. Pet. Sci. Eng.* **2020**, *195*, No. 107591.
(7) Chowdhury, S.; Shrivastava, S.; Kakati, A.; Sangwai, J. S. Comprehensive review on the role of surfactants in the chemical enhanced oil recovery process. *Ind. Eng. Chem. Res.* **2022**, *61*, 21−64.
(8) Gbadamosi, A. O.; Junin, R.; Manan, M. A.; Agi, A.; Yusuff, A. S. An overview of chemical enhanced oil recovery: recent advances and prospects. *Int. Nano Lett.* **2019**, *9*, 171−202.
(9) Druetta, P.; Raffa, P.; Picchioni, F. Plenty of Room at the Bottom: Nanotechnology as Solution to an Old Issue in Enhanced Oil Recovery. *Appl. Sci.* **2018**, *8*, 2596.
(10) Yang, Y.; Cheng, T.; Wu, H.; You, Z.; Shang, D.; Hou, J. Enhanced Oil Recovery Using Oleic Acid-Modified Titania Nanofluids: Underlying Mechanisms and Oil-Displacement Performance. *Energy Fuels* **2020**, *34*, 5813−5822.
(11) Hamad, H. T.; Al-Sharify, Z. T.; Al-Najjar, S. Z.; Gadooa, Z. A. A Review on Nanotechnology and Its Applications on Fluid Flow in Agriculture and Water Recourses. In *IOP Conference Series: Materials Science and Engineering*; IOP Publishing, 2020; Vol. *870*, p 012038.
(12) Mageswari, A.; Srinivasan, R.; Subramanian, P.; Ramesh, N.; Gothandam, K. M. Nanomaterials: Classification, Biological Synthesis and Characterization. In *Nanoscience in Food and Agriculture 3*; Springer, 2016; pp 31−71.
(13) Yekeen, N.; Kun, T. X.; Al-Yaseri, A.; Sagala, F.; Idris, A. K. Influence of critical parameters on nanoparticles-surfactant stabilized CO_2 foam stability at sub-critical and supercritical conditions. *J. Mol. Liq.* **2021**, *338*, No. 116658.
(14) Hou, J.; Du, J.; Sui, H.; Sun, L. A review on the application of nanofluids in enhanced oil recovery. *Front Chem. Sci. Eng.* **2022**, *16*, 1−33.
(15) Yekeen, N.; Salampessy, S. N.; Bakar, A. H. A.; Ali, M.; Okunade, O. A.; Musa, S. A.; Bavoh, C. B. Synthesis and pore-scale visualization studies of enhanced oil recovery mechanisms of rice straw silica nanoparticles. *J. Pet. Sci. Eng.* **2022**, No. 111292.
(16) Yekeen, N.; Khan, J. A.; Ali, M.; Elraies, K. A.; Okunade, O. A.; Ridha, S.; Al-Yaseri, A. Impact of nanoparticles−surfactant solutions on carbon dioxide and methane wettabilities of organic-rich shale and CO_2/brine interfacial tension: Implication for carbon geosequestration. *Energy Rep.* **2022**, *8*, 15669−15685.
(17) Joshi, D.; Maurya, N. K.; Kumar, N.; Mandal, A. Experimental investigation of silica nanoparticle assisted Surfactant and polymer systems for enhanced oil recovery. *J. Pet. Sci. Eng.* **2022**, *216*, No. 110791.
(18) Tavakkoli, O.; Kamyab, H.; Shariati, M.; Mohamed, A. M.; Junin, R. Effect of nanoparticles on the performance of polymer/surfactant flooding for enhanced oil recovery: A review. *Fuel* **2022**, *312*, No. 122867.
(19) Liu, D.; Zhang, X.; Tian, F.; Liu, X.; Yuan, J.; Huang, B. Review on nanoparticle-surfactant nanofluids: Formula fabrication and applications in enhanced oil recovery. *J. Dispersion Sci. Technol.* **2022**, *43*, 745−759.
(20) Al-Shatty, W.; Campana, M.; Alexander, S.; Barron, A. R. Interaction of Surface-Modified Alumina Nanoparticles and Surfactants at an Oil/Water Interface: A Neutron Reflectometry, Scattering, and Enhanced Oil Recovery Study. *ACS Appl. Mater. Interfaces* **2022**, *14*, 19505−19514.
(21) Yekeen, N.; Manan, M. A.; Idris, A. K.; Samin, A. M.; Risal, A. R. Experimental investigation of minimization in surfactant adsorption and improvement in surfactant-foam stability in presence of silicon dioxide and aluminum oxide nanoparticles. *J. Pet. Sci. Eng.* **2017**, *159*, 115−134.
(22) Lashari, N.; Ganat, T.; Elraies, K. A.; Ayoub, M. A.; Kalam, S.; Chandio, T. A.; Qureshi, S.; Sharma, T. Impact of nanoparticles stability on rheology, interfacial tension, and wettability in chemical enhanced oil recovery: A critical parametric review. *J. Pet. Sci. Eng.* **2022**, *212*, No. 110199.
(23) Yekeen, N.; Padmanabhan, E.; Idris, A. K.; Ibad, S. M. Surfactant adsorption behaviors onto shale from Malaysian formations: Influence of silicon dioxide nanoparticles, surfactant type, temperature, salinity and shale lithology. *J. Pet. Sci. Eng.* **2019**, *179*, 841−854.
(24) Yekeen, N.; Al-Yaseri, A.; Idris, A. K.; Khan, J. A. Comparative effect of zirconium oxide (ZrO_2) and silicon dioxide (SiO_2) nanoparticles on the adsorption properties of surfactant-rock system: Equilibrium and thermodynamic analysis. *J. Pet. Sci. Eng.* **2021**, *205*, No. 108817.
(25) Zargartalebi, M.; Barati, N.; Kharrat, R. Influences of hydrophilic and hydrophobic silica nanoparticles on anionic surfactant properties: Interfacial and adsorption behaviors. *J. Pet. Sci. Eng.* **2014**, *119*, 36−43.
(26) Saxena, N.; Kumar, A.; Mandal, A. Adsorption analysis of natural anionic surfactant for enhanced oil recovery: The role of mineralogy, salinity, alkalinity and nanoparticles. *J. Pet. Sci. Eng.* **2019**, *173*, 1264−1283.
(27) Kesarwani, H.; Sharma, S.; Mandal, A. Application of novel colloidal silica nanoparticles in the reduction of adsorption of surfactant and improvement of oil recovery using surfactant polymer flooding. *ACS Omega* **2021**, *6*, 11327−11339.
(28) Wu, Y.; Chen, W.; Dai, C.; Huang, Y.; Li, H.; Zhao, M.; He, L.; Jiao, B. Reducing surfactant adsorption on rock by silica nanoparticles for enhanced oil recovery. *J. Pet. Sci. Eng.* **2017**, *153*, 283−287.
(29) Yekeen, N.; Padmanabhan, E.; Syed, A. H.; Sevoo, T.; Kanesen, K. Synergistic influence of nanoparticles and surfactants on interfacial tension reduction, wettability alteration and stabilization of oil-in-water emulsion. *J. Pet. Sci. Eng.* **2020**, *186*, No. 106779.
(30) Briggs, N.; Raman, A. K. Y.; Barrett, L.; Brown, C.; Li, B.; Leavitt, D.; Aichele, C. P.; Crossley, S. Stable pickering emulsions using multi-walled carbon nanotubes of varying wettability. *Colloids Surf., A* **2018**, *537*, 227−235.
(31) Briggs, N. M.; Weston, J. S.; Li, B.; Venkataramani, D.; Aichele, C. P.; Harwell, J. H.; Crossley, S. P. Multiwalled carbon nanotubes at the interface of Pickering emulsions. *Langmuir* **2015**, *31*, 13077−13084.
(32) Chaturvedi, K. R.; Sharma, T. An Overview of the Application of Carbon Nanotubes for Enhanced Oil Recovery (EOR) and Carbon Sequestration. In *Carbon Nanotubes for a Green Environment*; Academic Press, 2022; pp 77−96.
(33) Alnarabiji, M. S.; Yahya, N.; Shafie, A.; Solemani, H.; Chandran, K.; Abd Hamid, S. B.; Azizi, K. The influence of hydrophobic multiwall carbon nanotubes concentration on enhanced oil recovery. *Procedia Eng.* **2016**, *148*, 1137−1140.

https://doi.org/10.1021/acs.energyfuels.3c00136
Energy Fuels 2023, 37, 5114−5129

(34) Razavinezhad, J.; Jafari, A.; Elyaderani, S. M. G. Experimental investigation of multi-walled carbon nanotubes assisted surfactant/polymer flooding for enhanced oil recovery. *J. Pet. Sci. Eng.* **2022**, *214*, No. 110370.
(35) Okunade, O. A.; Yekeen, N.; Padmanabhan, E.; Al-Yaseri, A.; Idris, A. K.; Khan, J. A. Shale core wettability alteration, foam and emulsion stabilization by surfactant: Impact of surfactant concentration, rock surface roughness and nanoparticles. *J. Pet. Sci. Eng.* **2021**, *207*, No. 109139.
(36) Li, X.; Pu, C.; Chen, X. A novel foam system stabilized by hydroxylated multiwalled carbon nanotubes for enhanced oil recovery: Preparation, characterization and evaluation. *Colloids Surf., A* **2022**, *632*, No. 127804.
(37) Li, X.; Pu, C.; Bai, Y.; Huang, F. Effect of surfactant types on the foam stability of multiwalled carbon nanotube stabilized foam. *Colloids Surf., A* **2022**, *648*, No. 129389.
(38) Lee, S. H.; An, J. H.; Kim, Y. J.; Lee, S. J. Electrically conductive foams via high internal phase emulsions with polypyrrole-modified carbon nanotubes: Morphology, properties, and rheology. *Polymer* **2022**, *242*, No. 124600.
(39) Yadav, P.; Gupta, S. M.; Sharma, S. A review on stabilization of carbon nanotube nanofluid. *J. Therm. Anal. Calorim.* **2022**, *147*, 6537−6561.
(40) Otumudia, E.; Hamidi, H.; Jadhawar, P.; Wu, K. The Utilization of Ultrasound for Improving Oil Recovery and Formation Damage Remediation in Petroleum Reservoirs: Review of Most Recent Researches. *Energies* **2022**, *15*, 4906.
(41) Haq, B.; Al Shehri, D.; Al Damegh, A.; Al Muhawesh, A.; Albusaad, M.; Lardhi, M.; Barri, A.; Iddris, A.; Muhammed, N.; Hossain, S. Z.; et al. The role of carbon nanotubes (CNTs) and carbon particles in green enhanced oil recovery (GEOR) for Arabian crude oil in sandstone core. *APPEA J.* **2020**, *60*, 133−142.
(42) Sircar, A.; Rayavarapu, K.; Bist, N.; Yadav, K.; Singh, S. Applications of nanoparticles in enhanced oil recovery. *Pet. Res.* **2022**, *7*, 77−90.
(43) Jafari, A.; Hasani, M.; Hosseini, M.; Gharibshahi, R. Application of CFD technique to simulate enhanced oil recovery processes: current status and future opportunities. *Pet. Sci.* **2020**, *17*, 434−456.
(44) Gharibshahi, R.; Jafari, A.; Ahmadi, H. CFD investigation of enhanced extra-heavy oil recovery using metallic nanoparticles/steam injection in a micromodel with random pore distribution. *J. Pet. Sci. Eng.* **2019**, *174*, 374−383.
(45) Yekeen, N.; Padmanabhan, E.; Idris, A. K. Synergistic effects of nanoparticles and surfactants on n-decane-water interfacial tension and bulk foam stability at high temperature. *J. Pet. Sci. Eng.* **2019**, *179*, 814−830.
(46) Ehtesabi, H.; Ahadian, M. M.; Taghikhani, V. Enhanced heavy oil recovery using TiO2 nanoparticles: investigation of deposition during transport in core plug. *Energy Fuels* **2015**, *29*, 1−8.
(47) Kuang, W.; Saraji, S.; Piri, M. A systematic experimental investigation on the synergistic effects of aqueous nanofluids on interfacial properties and their implications for enhanced oil recovery. *Fuel* **2018**, *220*, 849−870.
(48) Zallaghi, M.; Kharrat, R.; Hashemi, A. Improving the microscopic sweep efficiency of water flooding using silica nanoparticles. *J. Pet. Explor. Prod. Technol.* **2018**, *8*, 259−269.
(49) Gharibshahi, R.; Jafari, A.; Haghtalab, A.; Karambeigi, M. S. Application of CFD to evaluate the pore morphology effect on nanofluid flooding for enhanced oil recovery. *RSC Adv.* **2015**, *5*, 28938−28949.
(50) (a) Carman, P. C. Fluid flow through granular beds. *Chem. Eng. Res. Des.* **1997**, *75*, S32−S48. (b) Kozeny, J. *Uber Kapillare Leitung der Wasser in Boden*, Proc. Class I; Royal Academy of Science: Vienna, 1927; Vol. *136*, pp 271−306.
(51) Kozeny, J. *Uber Kapillare Leitung der Wasser in Boden*, Proc. Class I; Royal Academy of Science: Vienna, 1927; Vol. *136*, pp 271−306.
(52) Rostami, P.; Sharifi, M.; Aminshahidy, B.; Fahimpour, J. The effect of nanoparticles on wettability alteration for enhanced oil recovery: micromodel experimental studies and CFD simulation. *Pet. Sci.* **2019**, *16*, 859−873.
(53) Hemmat Esfe, M.; Esfandeh, S. 3D numerical simulation of the enhanced oil recovery process using nanoscale colloidal solution flooding. *J. Mol. Liq.* **2020**, *301*, No. 112094.
(54) Dezfuli, M. G.; Jafari, A.; Gharibshahi, R. Optimum volume fraction of nanoparticles for enhancing oil recovery by nanosilica/supercritical CO2 flooding in porous medium. *J. Pet. Sci. Eng.* **2020**, *185*, No. 106599.
(55) Ahmad, A.; Al-Dadah, R.; Mahmoud, S. CFD modelling of a novel liquid Nitrogen/Air engine and cryogenic heat exchanger for small scale applications. *Energy Procedia* **2017**, *142*, 3654−3660.
(56) Mahmoudi, S.; Jafari, A.; Javadian, S. Temperature effect on performance of nanoparticle/surfactant flooding in enhanced heavy oil recovery. *Pet. Sci.* **2019**, *16*, 1387−1402.
(57) Cheraghian, G.; Hendraningrat, L. A review on applications of nanotechnology in the enhanced oil recovery part A: effects of nanoparticles on interfacial tension. *Int. Nano Lett.* **2016**, *6*, 129−138.
(58) Feng, Y.; Hou, J.; Yang, Y.; Wang, S.; Wang, D.; Cheng, T.; You, Z. Morphology of MoS2 nanosheets and its influence on water/oil interfacial tension: A molecular dynamics study. *Fuel* **2022**, *312*, No. 122938.
(59) Wu, S.; Firoozabadi, A. Permanent alteration of porous media wettability from liquid-wetting to intermediate gas-wetting. *Transp. Porous Media* **2010**, *85*, 189−213.
(60) Ghalamizade Elyaderani, S. M.; Jafari, A. Investigation of interactions between silica nanoparticle, alkaline, and polymer in micromodel flooding for enhanced oil recovery. *Energy Sources, Part A* **2020**, 1−18.
(61) Ghalamizade Elyaderani, S. M.; Jafari, A.; Razavinezhad, J. Experimental investigation of mechanisms in functionalized multi-walled carbon nanotube flooding for enhancing the recovery from heavy-oil reservoirs. *SPE J.* **2019**, *24*, 2681−2694.
(62) Zhao, X.; Feng, Y.; Liao, G.; Liu, W. Visualizing in-situ emulsification in porous media during surfactant flooding: A microfluidic study. *J. Colloid Interface Sci.* **2020**, *578*, 629−640.
(63) Liu, Z.; Li, Y.; Luan, H.; Gao, W.; Guo, Y.; Chen, Y. Pore scale and macroscopic visual displacement of oil-in-water emulsions for enhanced oil recovery. *Chem. Eng. Sci.* **2019**, *197*, 404−414.
(64) Yang, Y.; Cheng, T.; Liu, H.; You, Z.; Hou, J. Oil Displacement Performance Using Bilayer-Coating Microspheres. *Ind. Eng. Chem. Res.* **2021**, *60*, 2300−2313.
(65) Nandwani, S. K.; Chakraborty, M.; Gupta, S. Chemical flooding with ionic liquid and nonionic surfactant mixture in artificially prepared carbonate cores: a diffusion controlled CFD simulation. *J. Pet. Sci. Eng.* **2019**, *173*, 835−843.
(66) Esfe, M. H.; Esfandeh, S.; Hosseinizadeh, E. Nanofluid flooding for enhanced oil recovery in a heterogeneous two-dimensional anticline geometry. *Int. Commun. Heat Mass Transf.* **2020**, *118*, No. 104810.

https://doi.org/10.1021/acs.energyfuels.3c00136
Energy Fuels 2023, 37, 5114−5129